Aerodynamic Analysis of a Scramjet Inlet and Isolator

Inês Cardoso
ines.cardoso@tecnico.ulisboa.pt

Instituto Superior Técnico, Lisboa, Portugal

December 2020

Abstract

Airbreathing engines, such as the supersonic combustion ramjet (or scramjet), promise a more sustainable solution for hypersonic flight than rocket powered engines, simply because they do not need to carry on-board oxidizer. This work uses an hypersonic CFD code to study the compression system of a scramjet engine designed for a trajectory point of Mach 10. An initial pre-analysis of a two-dimensional case study from the literature evidenced some discrepancies between the obtained values for pressure and those presented therein, but with a similar overall behaviour of the flow. It was found that lower wall temperatures benefit performance, whereas an adiabatic wall leads to impractically high temperatures. Chemical dissociation was found to be negligible, while the deployment of a two-temperature model showed that thermal non-equilibrium exists in a scramjet compression system, moderately impacting performance. Similar studies were then conducted for an axisymmetric geometry with the same compression and contraction ratios, with the main conclusion being that performance was worse for the axisymmetric case. Geometry parametric studies were conducted to verify how the number of ramps, the compression ratio, the isolator length, the contraction ratio and the expansion corner edge affected performance. An increased contraction ratio was found to favour inlet unstart for the two-dimensional geometry. Simulations at a trajectory point of Mach 7 were also conducted for both configurations and showed that it is possible to have a started inlet in this off-nominal regime, albeit at a decreased performance.

Keywords: Hypersonic, Scramjet, Computational Fluid Dynamics, Aerothermodynamics

1. Introduction

Hypersonic flow is characterized by the presence of high pressure and temperature gradients, thin shock layers and viscous interaction. Moreover, as speed increases, high-temperature effects arise, and with it physical phenomena such as chemical dissociation and ionization, as well as vibrational and chemical non-equilibrium, occur [1].

Among the vehicles capable of navigating in such a complex flow field, those equipped with airbreathing propulsion engines present a more sustainable choice for hypersonic flight than rocket powered engines. As the name suggests, these vehicles use the surrounding atmospheric air as oxidizer for the combustion processes, generating thrust [2], and thus eliminating the need to carry an on-board oxidizer and significantly increasing payload capabilities.

2. The Scramjet Engine

An hypersonic airbreathing engine, whose compression system relies on ram pressure, is designated a ramjet engine. Furthermore, if the mixing of the fuel with the hot air, and the consequent combustion, are carried out at supersonic speeds, the engine is designated a supersonic combustion ramjet, or scramjet, for short.

Ramjet and scramjet engines work under the same principles. First, a diffuser compresses the freestream air resulting in an increase of both ram pressure and temperature. Fuel is then mixed with the compressed air and combustion takes place. Finally, the high temperature exhaust is accelerated through a nozzle, generating thrust.

2.1. Compression system

The compression components provide, at the combustor entrance, the conditions necessary for efficient fuel combustion, with minimum aerodynamic losses. This is achieved through a series of oblique shock waves, that, when operating at the design Mach number for, all converge onto the tip of the engine cowl, yielding the so-called *shock-on-lip* condition. Furthermore, compression systems may present external, internal or mixed compression.

External compression systems (figure 1a) are self-starting and offer the possibility to operate at Mach numbers which are smaller than those for which they were designed for. This is accomplished through the spillage of flow when the shock-on-lip condition is not met, and is a desirable feature, since it offers a wider operational range. On the other hand, as a result of the angle between the freestream flow direction and the lip, these systems have high cowl drag.

For the case of internal compression systems (figure 1b), a series of symmetrical oblique yield a uniform and parallel internal flow, and allows for a shorter axial length than that of external compression systems. Spillage is, however, not possible, which means that, for a fixed geometry, these systems cannot stray far from their design Mach number.

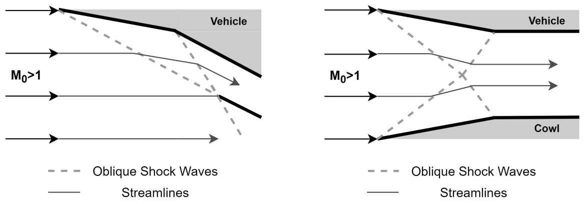

(a) External compression (b) Internal compression

Figure 1: Schematics of the different compression systems. Adapted from [2, 3].

Mixed compression systems are usually preferred, since they take advantage of both internal and external compression, and result in a design that can operate below the design Mach number, with significantly less cowl drag than that of external compression systems. They present, however, an axial length that must be greater than that of the other two types of compression systems.

It is also important to notice that neither of the compression systems presented above should operate above their design Mach number, since this operating condition results in high heat loads and flow instabilities, thus presenting the risk of material failure [3].

2.2. Isolator

The isolator is a constant area diffuser placed between the compression system and the combustion chamber. Inside this component, pressure increases in a controlled manner by means of an oblique shock train that continuously interacts with the boundary layer, allowing the flow to adjust to the back pressure imposed by the downstream components. The main consideration regarding this component is that it should be long enough to contain the entire shock train and prevent inlet unstart [2, 4].

2.3. Combustion Chamber and Expansion System

As the air leaves the isolator it enters the combustion chamber. Here, fuel is injected, appropriate mixing is achieved, and supersonic combustion takes place, all of which must be accomplished within a reasonable length [2].

At the expansion system, or nozzle, the exhaust is accelerated to high velocities, generating forward thrust. Not unlike the compression system, this component typically has an internal flow, that then continues to expand in the vehicle aftbody, in an unconfined external flow.

3. Literature Review

While literature states that scramjet operating limits range from Mach 4 to Mach 15 [5], Urzay [6] suggests that hypersonic cruising trajectories which take place at lower Mach numbers, ranging from 6 to 10, lead to more manageable loads (both thermal and mechanical), as well as reduced high temperature effects.

3.1. Trajectory Point

While an hypersonic airbreathing vehicle cannot operate at freestream velocities that are higher than that for which it was designed for, it can, however, operate at freestream Mach numbers which are lower than its design Mach number, as long as spillage can occur. Therefore the vehicle should be designed for flight conditions corresponding to the maximum Mach number at which it is expected to operate, which is to say, Mach 10.

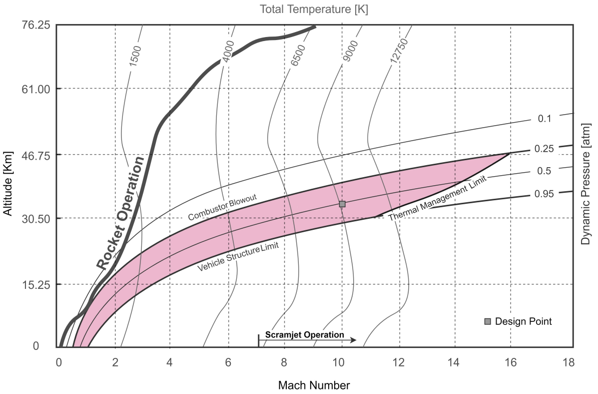

Figure 2: Flight corridor for an hypersonic airbreathing engine as function of Mach number, altitude and dynamic pressure. Selected trajectory point are reported. Adapted from [7].

The set of feasible trajectory points, or flight corridor, for airbreathing propulsion engines is limited by the severe flight conditions that arise due to high mechanical and thermal loads. One parameter that helps assessing whether a given trajectory point is within the flight corridor or not is the dynamic pressure q. On the one hand, if the dynamic pressure is too low, the wing area required for sustainable flight is unreasonably high; on the other hand, if q is too high, the aerodynamic and/or structural forces acting on the vehicle may lead to material failure. Figure 2, from which a feasible trajectory point was selected, identifies the limits of the flight corridor for an hypersonic airbreathing engine, as a function of the freestream Mach number, altitude and dynamic pressure.

The selected trajectory point, for a freestream Mach number of 10, is within the feasible region, at a dynamic pressure of 50kPa, a compromise between the low and high dynamic pressures that bound the flight corridor, at an altitude of 33km.

3.2. Case Study

Reference [3] provides a methodology for a compression system design, based on oblique-shock theory, as well as its application to a compression system whose operating design point corresponds to Mach 10. The geometry consists of a mixed compression inlet, of the form presented in figure 3, with values of θ_1, θ_2, H and H/h given in table 1.

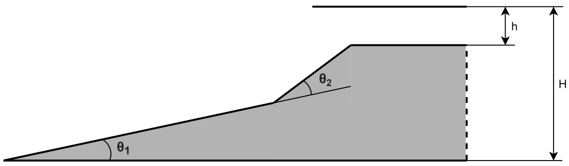

Figure 3: Schematics of a mixed compression system.

$\theta_1[°]$	$\theta_2[°]$	H [m]	H/h
6.5	8.4	0.250	10

Table 1: Baseline design for the two-dimensional compression system [3].

Additionally, reference [3] considers an isolator length, L, of 0.5m. This length is defined by the back pressure necessary for ignition to occur, and, for a combustor entry velocity of 2.4km/s and temperatures above 1000K, reference [8] shows that a back pressure of circa 50kPa results in an acceptable combustor length. While this value presents ideal conditions for combustion, only combustor entry pressures below 20kPa were considered to impede ignition [9].

4. Mathematical Formulation

To account for all phenomena that characterise hypersonic flow, several considerations had to be made. The first of which was to consider the gas as a mixture of several chemical species, particularly, the gas was considered to be a mixture of N_2, O_2, N, O and NO.

Furthermore, the high temperatures found within a scramjet engine were also considered to give rise to chemical reactions and therefore the formation and consumption of the different species must be accounted for in the governing equations.

Lastly, the different particles' thermal energy modes were accounted for by considering Park's two temperature model for thermal non-equilibrium, which assumes that the temperature of the translational and rotational energy modes is the same, while the temperature of the vibrational energy mode is in equilibrium with the electronic energy mode.

The set of governing equations for the flow is presented in equations 1 through 4.

$$\frac{\partial(\rho c_s)}{\partial t} + \nabla\cdot(\rho c_s \mathbf{u}) = \nabla\cdot J_s + \dot{\omega}_s, \tag{1}$$

$$\frac{\partial(\rho \mathbf{u})}{\partial t} + \nabla\cdot(\rho \mathbf{u}\otimes\mathbf{u}) = \nabla\cdot[\tau] - \nabla p, \tag{2}$$

$$\frac{\partial(\rho e)}{\partial t} + \nabla\cdot(\rho \mathbf{u} h) = \nabla\cdot(\mathbf{u}\cdot[\tau]) - \nabla\cdot\mathbf{q} - \nabla\cdot(p\mathbf{u}), \tag{3}$$

$$\frac{\partial(\rho e_k)}{\partial t} + \nabla\cdot(\rho \mathbf{u} h_k) = \nabla\cdot\left(-k_k\nabla T_k + \sum_s J_s h_{s,k}\right) + \dot{\Omega}_k. \tag{4}$$

Of the equations above, equation 1 is the mass conservation equation, where ρ is the density, c_s is the mass fraction of species s, and $\mathbf{u}$ is the flow velocity vector. J_s is the mass diffusion flux vector, given by Fick's law (eq. 5) and $\dot{\omega}_s$ is the rate of formation or consumption of species s.

$$J_s = \rho D_s \nabla c_s. \tag{5}$$

Equation 2 is the momentum conservation equation, where p is the pressure and $[\tau]$ is the viscous stress tensor, given by equation 6, where μ is the dynamic viscosity coefficient and $[\mathrm{I}]$ is the identity matrix.

$$[\tau] = \mu(\nabla\mathbf{u} + (\nabla\mathbf{u})^{\mathrm{T}}) - \frac{3}{2}\mu(\nabla\mathbf{u})[\mathrm{I}]. \tag{6}$$

Equation 3 is the total energy conservation equation, where e is the total internal energy per unit mass and $\mathbf{q}$ is the heat flux vector, given by equation 7, where k_k and T_k are, respectively, the thermal conductivity and temperature associated with the thermal energy mode k, h_s is the enthalpy of species s and $\mathbf{q}_R$ is the radiative heat flux vector [1].

$$\mathbf{q} = -\sum_k k_k\nabla T_k + \sum_s J_s h_s + \mathbf{q}_R. \tag{7}$$

Lastly, equation 4 is the non-equilibrium thermal energy conservation equation, where $\dot{\Omega}_k$ is the energy-exchange source term associated with the thermal energy mode k.

4.1. Transport Coefficients

Dissipative fluxes govern mass, momentum and energy transport and are necessary to adequately describe the behaviour of the flow with respect to concentration, velocity and temperature gradients, respectively. To that end, it is necessary to calculate the values of the multi-component transport coefficients. In this work, the Wilke/Blottner/Eucken model, which is expected to yield reasonable results for low levels of ionization, and temperatures that do not exceed 10000K [10], has been considered. It yields equations 8 and 9 for the dynamic viscosity and thermal conductivity of a mixture, respectively.

$$\mu = \sum_s \frac{x_s \mu_s}{\phi_s}, \tag{8}$$

$$k_k = \sum_s \frac{x_s k_{k,s}}{\phi_s}. \tag{9}$$

Regarding the equations above, x_s is the mole fraction of species s and ϕ_s is a scale factor which depends on the dynamic viscosities μ_s and molar masses M_s of the interacting species. Furthermore, the viscosity of a given species is given by Blottner's curve fitting model [11], whereas the thermal conductivity is given by Eucken's relation [12]. Here, we assume $\mathsf{Le} = 1$. Lastly, the mass diffusion coefficient is given by equation 10, and is assumed equal for all species.

$$D_s = D = \frac{\mathsf{Le}\ k}{\rho c_p}, \tag{10}$$

where Le is the Lewis number, which measures the ratio of thermal diffusivity to mass diffusivity, and c_p is the gas mixture specific heat at constant pressure.

4.2. Oblique Shock Wave Theory

Owing to its simplicity, oblique shock wave theory was used to pre-dimension the different inlets considered.

For the the case of the axisymmetric compression system, the Taylor Maccoll analysis was employed alongside the oblique shock wave theory.

4.3. Performance Parameters

For the purpose of assessing performance, cross-section averaged values of the different quantities were used, under the assumption that the flow is mixed into a uniform, one-dimensional state. Equations 11 through 13 present the selected parameters to evaluate performance.

$$\pi_c = \frac{p_c}{p_\infty} \left\{ \frac{1 + \frac{\gamma-1}{2}\mathsf{Ma}_c^2}{1 + \frac{\gamma-1}{2}\mathsf{Ma}_\infty^2} \right\}^{\frac{\gamma}{\gamma-1}}, \tag{11}$$

$$\eta_{\mathsf{KE}} = 1 - \frac{2}{(\gamma-1)\mathsf{Ma}_\infty^2} \left\{ \frac{T_c}{T_\infty} \left(\frac{p_c}{p_\infty} \right)^{-\frac{\gamma-1}{\gamma}} - 1 \right\}. \tag{12}$$

$$\eta_c = \frac{(T_c/T_\infty) - (T_c/T_\infty)(p_c/p_\infty)^{-\frac{\gamma-1}{\gamma}}}{(T_c/T_\infty) - 1}. \tag{13}$$

Equation 11 gives the total pressure ratio π_c, equation 12 gives the kinectic energy efficiency and equation 13 gives the compression efficiency. For all these equations, the subscript ∞ stands for freestream conditions, whereas the subscript c stands for conditions at the isolator exit (or combustor entry).

The mass flow rate ratio was also considered a useful parameter to address the amount of spillage that occurs and was therefore calculated alongside the rest of the performance parameters.

5. Numerical Implementation

The numerical implementation of the problem consisted of identifying suitable boundary conditions, as well as an appropriate mesh for the problem at hand. Table 2 presents the atmospheric conditions for the selected trajectory point corresponding to freestream conditions of Mach 10, considered as the upstream boundary condition.

Ma	u[km/s]	p[Pa]	T[K]	x_{N_2}	x_{O_2}
10	3.11	714	240	0.79	0.21

Table 2: Upstream conditions at an altitude of 33km and a dynamic pressure of 50kPa.

In terms of wall boundary conditions, a no-slip, fully catalytic wall, with a temperature set to 1465K was chosen, to ensure that we are within the thermal management limit. Lastly, the outlet boundary condition was chosen as supersonic, where the properties are extrapolated from the interior domain.

Figure 4 presents a schematics of the considered physical domain for the two-dimensional configuration, with the applied boundary conditions clearly identified.

A grid convergence study was conducted, of which four different grid resolutions were considered (115x28, 175x40, 175x60 and 250x60). All of these grids presented a near wall refinement in order to capture boundary layer behaviour (as presented in figure 4), however, as seen in figure the applied refinement was not sufficient for the coarser grid, and this resolution was discarded for further use.

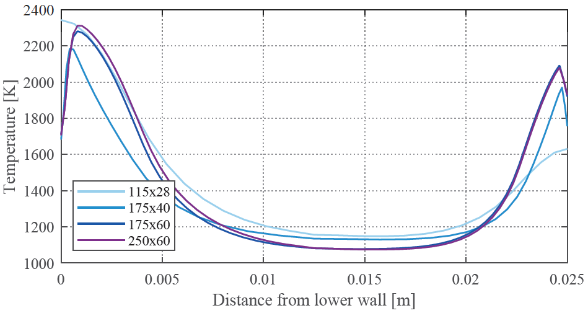

Figure 6: Temperature at the isolator exit, used for the mesh convergence study of the two-dimensional configuration.

The remaining grids were compared in terms of temperature and velocity profiles at the isolator exit, since these are key parameters for enabling supersonic combustion, and in terms of oblique

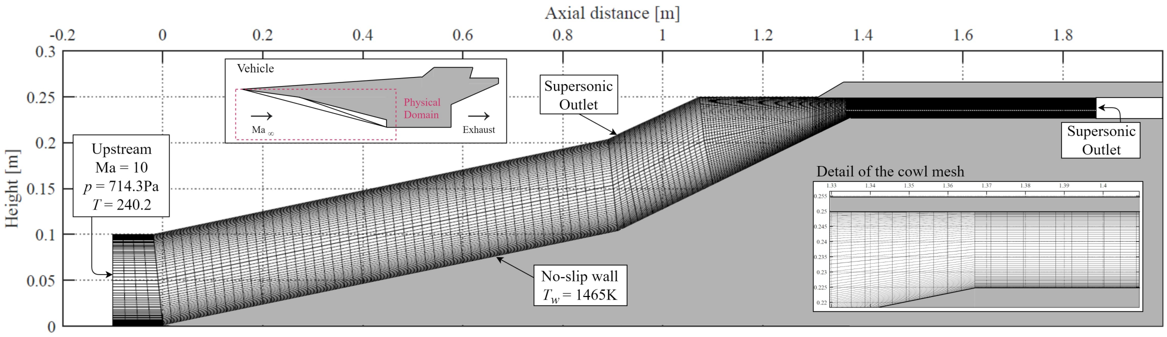

Figure 4: Two-dimensional compression system mesh and boundary conditions. Not to scale.

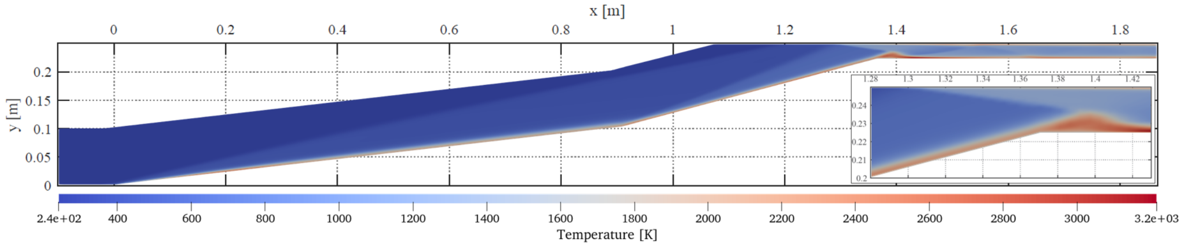

Figure 5: Temperature field obtained for the viscous frozen-flow simulation of the two-dimensional compression system.

shock position. Figure 6 presents the temperature profiles at the isolator exit for the considered grids, and shows that, although the 175x40 resoltuion is capable of capturing boundary layer behaviour, it still presents an error relative to the finer meshes. On the other hand, the 175x60 grid configuration presents a temperature profile similar to the one obtained for the 250x60 resolution, at a much lesser computational cost. For this reason, the 175x60 grid was favoured over the 250x60 one.

A similar grid convergence study was conducted for the axisymmetric configuration with the design parameters of table 3, which ensure the same contraction and compression ratio as the ones of the two-dimensional configuration. For this configuration the 230x60 grid was retained.

$\vartheta_1\,[°]$	$\vartheta_2\,[°]$	H [m]	H/h
8.6	11.3	0.250	10

Table 3: Design parameters for the baseline axisymmetric compression system.

6. Results

6.1. Two-dimensional configuration

The temperature field obtained for the frozen flow solution of the two-dimensional configuration is presented in figure 5. This figure shows that, instead of converging to the cowl tip, the oblique shock waves generated by each of the compression system ramps present a wave angle that is higher than predicted by oblique shock wave theory, resulting in flow spillage and in the absence of the shock-on-lip condition. This is in good agreement with the literature and, according to [3] this is a consequence of the thickness of the viscous boundary layer and is a desirable effect since it avoids a hot spot on the cowl tip. The flow within the isolator, on the other hand, behaves as expected. At the entry, the flow expands, resulting in flow separation and in the formation of a small recirculation zone; then, a shock train forms, across which pressure increases in a controlled manner.

Discrepancies between the obtained results and the ones presented in the literature were also found, in terms of peak pressure at the cowl tip, which was 78006Pa, circa 4.87% less than the value presented in reference [3]. Furthermore, in the same reference, it is stated that the available pressure for combustion is greater than 50kPa, however, for the present simulation, the isolator exit pressure had a maximum value of 42039Pa, and an average pressure of 38961Pa. Since there were some differences between the modelled problem and the one from the literature, namely in terms of turbulence model and the wall temperature was not clearly reported in reference [3], this was found to be an acceptable deviation. Accordingly, to estimate the influence of wall temperature, it was deemed of interest to study its effects on the behaviour of the flow within the compression system.

Figure 7 presents the isolator exit temperature profile for wall temperatures of 1465K and 745K, as well as for an adiabatic wall, and shows that, while nearly halving the chosen wall temperature does not significantly alter the obtained temperature profile, the choice of an adiabatic wall boundary condition leads to unreasonably high temperatures, past most material working temperatures, and thus violating the thermal management limit.

Figure 8 presents a detail of the thermal boundary layer at the isolator entry, to emphasise the

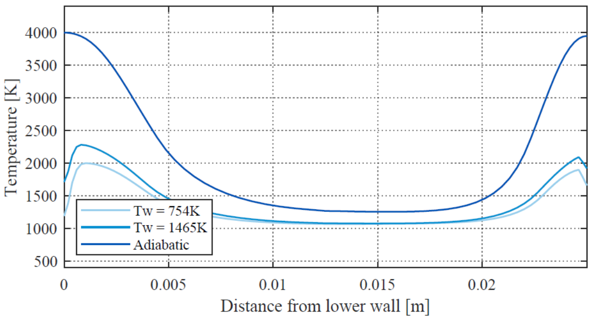

Figure 7: Temperature profiles at the isolator exit for different wall boundary conditions, for the two-dimensional configuration.

repercussions of setting an adiabatic wall boundary condition. An increase of the thickness of the boundary layer and separation region is shown, which contributes to total pressure loss and reduces the available mass flow at the combustor entrance.

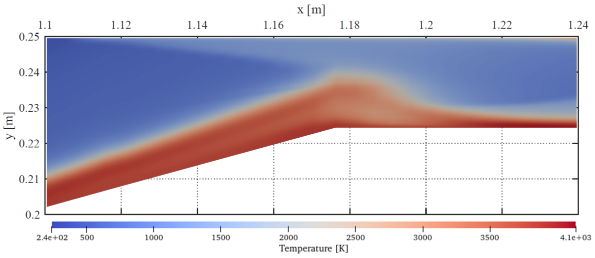

Figure 8: Detail of the thermal boundary layer for the adiabatic wall boundary condition, for the two-dimensional configuration.

The performance parameters and mass flow rate ratios for the different considered wall temperatures are presented in table 4, where it shown that lower wall temperatures result in higher performance figures, whereas an adiabatic wall means worse performance, and reduces the mass flow rate ratio by nearly 10% when compared to the baseline case ($T_w = 1465$K).

Case	π_c	η_{KE}	η_c	$\dot{m}_c/\dot{m}_\infty$
$T_w = 1465$K	0.0793	0.9442	0.7898	0.7921
$T_w = 745$K	0.0908	0.9495	0.7956	0.8127
Adiabatic	0.0332	0.9035	0.7661	0.6925

Table 4: Performance parameters dependence on wall temperature for the two-dimensional configuration.

Reactive and thermal non-equilibrium flows

As previously stated, an expected outcome of hypersonic flows subject to high temperature effects is chemical dissociation and/or thermal non-equilibrium. To address these effects, Park's kinetic [13] and two-temperature [14] models were used. Figure 9 presents the O and NO mass fractions at the isolator exit, obtained from the chemically reacting flow solution, whereas figure 10 presents the temperature profiles at the same location, for the case of thermal non-equilibrium.

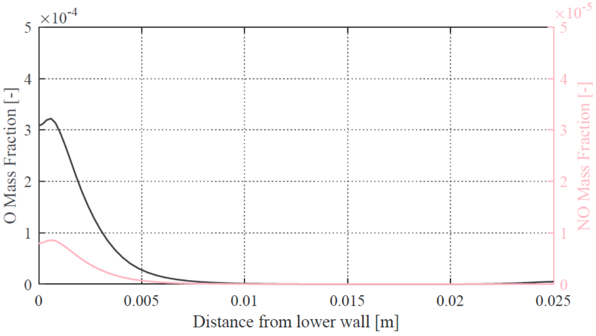

Figure 9: O and NO mass fractions obtained at the isolator exit, for the reactive flow, for the two-dimensional configuration.

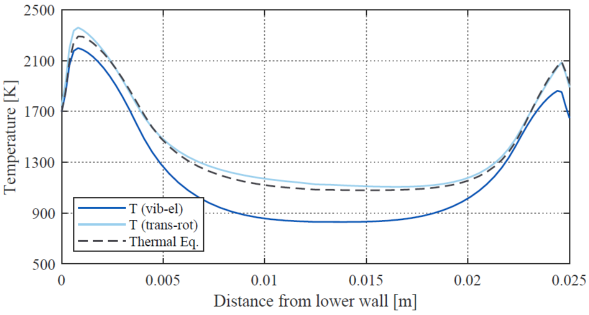

Figure 10: Temperature profiles, at the isolator exit, for thermal equilibrium and non-equilibrium, for the two-dimensional configuration.

For the reactive flow solution, non-negligible dissociation of molecular oxygen and formation of nitric oxide was observed. However, this impacted minimally the computed pressure and temperature profiles. This means that it might not be worth it to spend computational resources on the calculation of the chemically reacting flow. Nonetheless, because NO contributes to the formation of smog and the destruction of the ozone layer it is important to be aware of its potential formation.

Thermal non-equilibrium was also found at the isolator exit, with translational-rotational and vibrational-electronic temperatures that differ by a maximum of 309K at the flow core. Furthermore, the peak translational-rotational temperature at the lower wall boundary layer is higher than the equilibrium peak-temperature by 2.88%. If thermal non-equilibrium is considered, the obtained pressure profile was also found to be different than the one obtained for the frozen and reactive flow solutions, a result which will impact the obtained performance parameters, presented in table 5.

Case		π_c	η_{KE}	η_c	$\dot{m}_c/\dot{m}_\infty$
Thermal Eq.	Frozen	0.0793	0.9442	0.7898	0.7921
	Reactive	0.0781	0.9440	0.7897	0.7916
Thermal Non-equilibrium		0.0652	0.9596	0.8183	0.7858

Table 5: Performance parameters obtained for reactive and thermal non-equilibrium flows (two-dimensional configuration).

Since chemical dissociation does not significantly alter the property profiles at the isolator exit, the performance parameters obtained for the frozen and reactive flows are very similar. Contrarily, the total pressure ratio decreases for the thermal non-equilibrium case, however the kinetic energy efficiency as well as the the compression efficiency increase when thermal non-equilibrium is considered. Lastly, when thermal non-equilibrium was taken into account, the mass flow rate ratio is found to be slightly lower (circa 0.5%).

6.2. Axisymmetric Configuration

The obtained temperature field for the frozen flow solution of the axisymmetric configuration is presented in figure 11, and shows that while spillage occurs for the case of an axisymmetric configuration, it is not as significant as it was for the two-dimensional case. On the other hand, since, for the case of hypersonic flow around a conical surface, properties vary with distance to the cone surface, and to ensure that the imposed compression ratio is achieved for the entire physical domain, the obtained pressures after the second oblique shock were higher than those obtained for the two-dimensional flow. This is particularly distinguishable at the cowl tip, where the pressure peaks at 105282Pa, 35% more than the value obtained for the two-dimensional configuration in the same location. Another remark regarding the axisymmetric configuration concerns the isolator exit pressure. Figure 12 plots the isolator exit pressure for the two-dimensional and axisymmetric configurations.

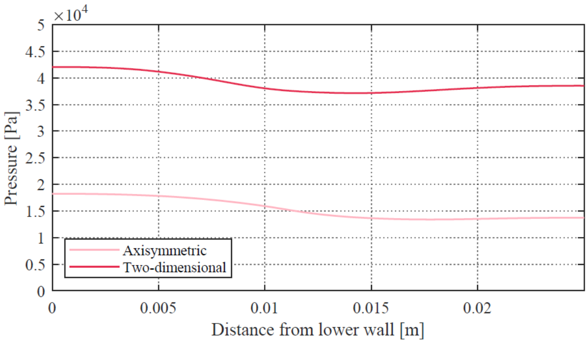

Figure 12: Isolator exit profile for the two-dimensional and axisymmetric compression systems.

While a contraction ratio H/h of 10 ensures, for the two-dimensional configuration, an average isolator exit pressure that falls just short to the ideal pressure for supersonic combustion, the average pressure at the same location, for the axisymmetric configuration, is only 15360Pa, which is less than the approximate 20kPa that reference [9] deems necessary for ignition to occur.

Concerning chemically reacting and thermal non-equilibrium flow descriptions, the axisymmetric configuration yielded very similar results to the ones previously presented for the two-dimensional configuration, i.e. small traces of O and NO were found to be present at the isolator exit, and thermal non-equilibrium was found to occur, with translational-rotational and vibrational-electronic temperatures that differ by a maximum of 431K at the flow core. The impact of these results on performance is also identical to the one encountered for the two-dimensional configuration, as shown in table 6.

Case		π_c	η_{KE}	η_c	$\dot{m}_c/\dot{m}_\infty$
Thermal Eq.	Frozen	0.0327	0.9181	0.6833	0.6276
	Reactive	0.0305	0.9172	0.6803	0.6068
Thermal Non-equilibrium		0.0243	0.9492	0.7274	0.5906

Table 6: Performance parameters obtained for the thermal equilibrium and non-equilibrium solutions for the axisymmetric configuration.

Comparing the results of table 6 with those of table 5, the performance parameters and mass flow rate ratios were always smaller for the axisymmetric configuration.

6.3. Geometry Parametric Study

The geometry parametric study consisted on a variation of the number of ramps, the compression ratio, the isolator length, the contraction ratio, and the shape of the expansion corner for the two dimensional configuration. For the axisymmetric configuration, only the variation of the contraction ratio was expected to present different results, hence it was the only considered geometry variation.

Variation of the number of ramps

The three-ramp geometry of reference [3] was used to study the influence of a greater number of ramps. Table 7 presents the design parameters for this geometry. The chosen grid for this geometry is the same than the one previously defined (175x60), with the same grid resolution at the isolator.

θ_1 [°]	θ_2 [°]	θ_3 [°]	H [m]	H/h	L [m]
4.3	5.0	6.0	0.250	10	0.5

Table 7: Design parameters for a two-dimensional compression system with three ramps.

The main difference between the two and three ramp inlets is the pressure at the isolator entry, which increases to 90810Pa at this location. This result too presents a relative error with respect to the results of the literature [3] by about 9%. Once more, this difference is expected to be a result of the identified discrepancies between how the problem was modelled in this work and in the literature (wall temperature and turbulence modelling). Regarding the isolator exit, increasing the number of ramps slightly shifted the angle of the reflected shock waves at the isolator and resulted in

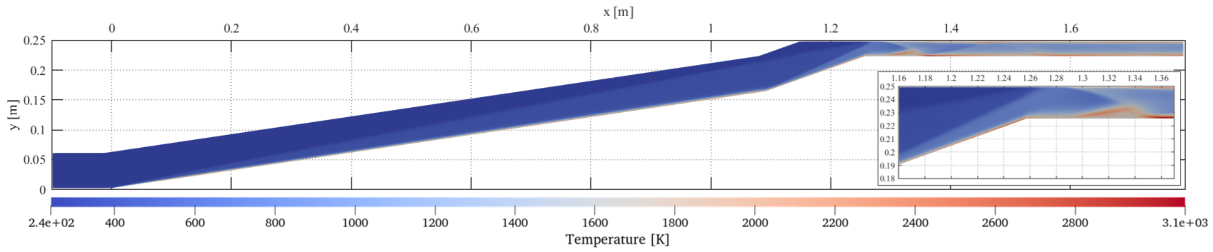

Figure 11: Temperature field obtained for the viscous (Navier-Stokes) frozen-flow simulation of the axisymmetric compression system.

a shifted pressure profile, but this did not significantly change the maximum or average pressures at this location. Performance, on the other hand, was affected by the choice of a three ramp inlet, with better performance parameters obtained for this geometry (table 8), a result which is also predicted in reference [3].

Case	π_c	η_{KE}	η_c	$\dot{m}_c/\dot{m}_\infty$
Three Ramp	0.0813	0.9449	0.7906	0.8061

Table 8: Performance parameters obtained for a three-ramp inlet, for the two-dimensional configuration.

Variation of the compression ratio

A change in the compression ratio can be obtained by varying the angle of the ramps. The case study of reference [3] consisted of a compression ratio of 4 across each of the first two oblique shock waves (PRat = 4). Table 9 presents the design parameters for an equivalent compression system with a compression ratio of 5 (PRat = 5).

$\theta_1\,[^\circ]$	$\theta_2\,[^\circ]$	H [m]	H/h
7.9	10.7	0.250	10

Table 9: Design parameters for a two-dimensional compression system with a compression ratio of 5.

Increasing the compression ratio increases the average pressure at the isolator exit from 38961Pa to 48245Pa, which comes at cost of a higher temperature at this location, and therefore augmenting the risk of crossing the thermal management limit. Furthermore, a thicker recirculation bubble was also obtained for this geometry. As explained for the case of an adiabatic wall, this increases total pressure loss and contributes to flow blockage, which is reflected in the performance parameters of table 10.

Case	π_c	η_{KE}	η_c	$\dot{m}_c/\dot{m}_\infty$
PRat = 5	0.0489	0.9317	0.7878	0.7859

Table 10: Performance parameters obtained for the different number of ramps, for the two-dimensional configuration.

Variation of the isolator length

It has been previously stated that inside the isolator pressure increases in a controlled manner, by means of an oblique shock train. Logically, increasing the length of the shock train should result in a higher exit pressure. However, figure 13, which plots the pressure along the centerline of the isolator, for an isolator length of 1m, shows that there is a limited amount of pressure increase that can be attained by simply increasing the length of this component. This is a result which is in good agreement with the literature [2].

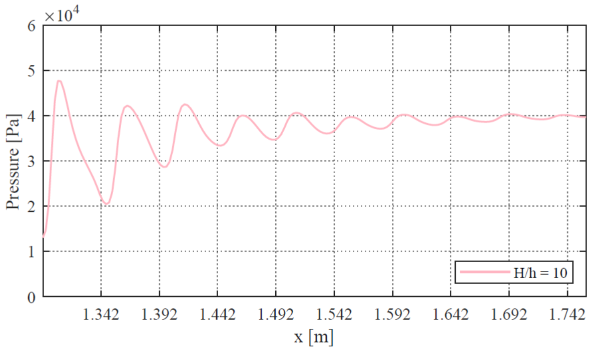

Figure 13: Pressure along the centerline of the isolator, for an isolator length of 1m, for the two-dimensional configuration.

Conditions at x = 1.517m (corresponding to an isolator length of 0.15m), at x = 1.867 (corresponding to the baseline design) and at x = 2.376 (corresponding to an isolator length of 1m) were considered to assess how performance is affected by isolator length. The obtained results are presented in table 11, where it is shown that a shorter isolator length presents better performance figures. This however comes at the cost of having a less uniform flow at the combustor, since, close to the isolator entry, the flow is still highly influenced by the impinging shock waves.

Case	π_c	η_{KE}	η_c	$\dot{m}_c/\dot{m}_\infty$
L = 0.15m	0.0983	0.9464	0.7919	0.8136
L = 0.5m	0.0793	0.9442	0.7898	0.7921
L = 1m	0.0697	0.9439	0.7915	0.7909

Table 11: Performance parameters obtained for the different isolator lengths, for the two-dimensional configuration.

Two-dimensional configuration: variation of H/h

The contraction ratio can be varied by varying the isolator height. One must recall, however, that the Mach number at the combustor entry must be greater than unit, for supersonic combustion to occur. To that end, a maximum contraction ratio was calculated through the empirical Kantrowitz limit

[15] reported in equation 14. This equation yields a maximum H/h of 28.986 for a freestream Mach number of 10.

$$\left\{\frac{\mathrm{h}}{\mathrm{H}}\right\}_{\mathrm{max}} = 0.05 - \frac{0.52}{\mathrm{Ma}_\infty} + \frac{3.65}{\mathrm{Ma}_\infty^2} \tag{14}$$

With respect to the maximum contraction ratio, a geometry with a value of H/h $= 15$ was considered, which gives an isolator height of 0.0167m. For this height, the oblique shock wave generated at the cowl tip reflected on the second ramp, upstream the isolator entry (figure 14).

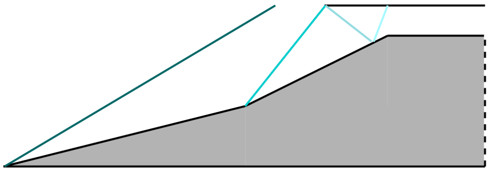

Figure 14: Schematics of the shock wave structure for a contraction ratio of 15, for the two-dimensional configuration.

As a consequence of this reflection, and in light of the increased proximity between the cowl and the ramp wall, an interaction between the shocks and the boundary layer led to the formation of a vortex at the entrance to the isolator. This caused the separation bubble to oscillate back and forth, in what was identified as inlet buzzing [16, 17]. This further results in the distortion of the flow inside the isolator, which causes inlet unstart, i.e. impedes the normal operation of the inlet.

Absence of an expansion corner edge

To address flow separation, a workaround has been tested: rather than having a clearly defined edge, a rounded corner, of radius 0.155m, was considered. Figure 15 presents a detail of the velocity field at the isolator entry, when a rounded corner was considered.

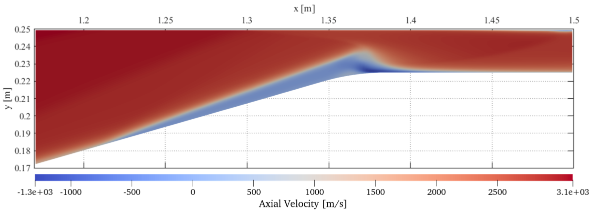

Figure 15: Detail of the velocity field, at the isolator entry, for a rounded corner, for the two-dimensional configuration.

As shown in figure 15, the flow separates earlier, resulting a thicker separation bubble at the isolator entry. Furthermore, the separation region behaves as a third ramp that generates an additional shock wave, increasing the obtained compression, but also the temperature within the isolator. This adversely affects the performance parameters of table 12, with all three performance parameters being lower for this configuration.

Case	π_c	η_{KE}	η_c	$\dot{m}_c/\dot{m}_\infty$
Without edge	0.0598	0.9362	0.7869	0.7838

Table 12: Performance parameters for the rounded corner, for the two-dimensional configuration.

While this cannot be taken for granted, turbulence is known to delay separation, which means that, considering a turbulence model, this geometry might have evidenced better performance than the geometry with a clearly defined edge.

Axisymmetric configuration: variation of H/h

As previously discussed, only the variation of the contraction ratio is expected to yield different results than the ones presented for the two-dimensional geometries. This is mostly due the separation bubble lying downstream of the isolator entry for the baseline contraction ratio (figure 11). This means that there is still a comfortable margin for increasing the contraction ratio without risking inlet unstart. To that end, contraction ratios of 15 and 25 were considered.

Figure 16 plots the pressure along the isolator centreline, for the different contraction ratios. Expectedly, an increase of compression leads to an increase of the frequency at which the shock waves reflect inside the isolator. This, in turn, results in an increase of the isolator exit pressure and temperature. Figure 16 further shows that, for the case of the highest contraction ratio, the pressure does not significantly increase for the second half of the isolator length, which may mean that this geometry doesn't require such a long isolator. Another consequence of having a smaller isolator is that the recirculation bubble is moved towards the entry, although even for the highest contraction ratio chosen it remained within the isolator.

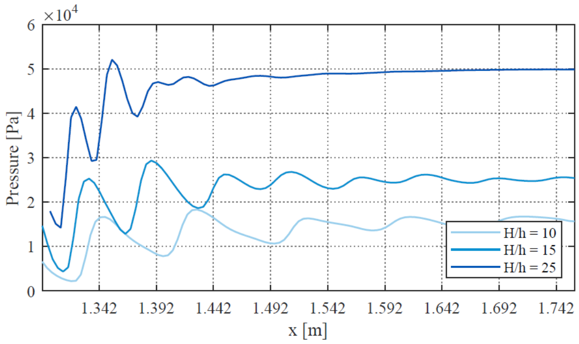

Figure 16: Pressure along the isolator centreline, for different contraction ratios, for the axisymmetric configuration.

The impact of the isolator height on the performance parameters is given in table 13, which shows that, an increase in contraction ratio yields an increase in performance. However, this does not necessarily translate in terms of mass flow rate ratio (note that both presented mass flow rate ratios are lower than the one obtained for the baseline contraction ratio).

Case	π_c	η_{KE}	η_c	$\dot{m}_c/\dot{m}_\infty$
H/h = 15	0.0350	0.9226	0.7285	0.5885
H/h = 25	0.0382	0.9314	0.7913	0.5975

Table 13: Performance parameters for the considered isolator heights for the axisymmetric configuration.

6.4. Off-Design Conditions

Off-design performance of the vehicle at Mach 7 and a dynamic pressure of 50kPa was also analysed. For this case, the considered physical domain had to include all y coordinates up to 0.25m to account for the variation of the first oblique shock wave angle. Nonetheless, the grid was kept at 175x60 and 230x60 total cells for the two-dimensional and axisymmetric configurations, respectively, to maintain the same isolator resolution. The obtained performance parameters are presented in table 14, wherein the results for a freestream Mach number of 10 were recalculated for the adapted grid to allow for a better comparison.

Case	Mach	π_c	η_{KE}	η_c	$\dot{m}_c/\dot{m}_\infty$
2D Plan.	10	0.0833	0.9458	0.7880	0.7718
	7	0.0896	0.8920	0.7370	0.4381
2D Axi.	10	0.0358	0.9316	0.7920	0.5922
	7	0.0884	0.8914	0.7350	0.3355

Table 14: Performance parameters obtained at Mach 7 and Mach 10 freestream conditions.

Table 14 shows that the total pressure ratio increases for a freestream Mach number of 7, while all other performance parameters decrease, with mass flow rate ratios nearly halved. Nevertheless, a variable geometry might help increase this value.

7. Conclusions

The main focus of this work was the study of the flow within a scramjet inlet and isolator. The reproduction of a case study from the literature showed that the thick boundary layer increases the angle of the oblique shock waves, generating spillage for the design point Mach number. Furthermore, lower wall temperatures were found to benefit performance. Chemistry and non-equilibrium effects were also found to slightly change the flow properties at the isolator exit. The study of an axisymmetric inlet yielded similar results, having shown worse performance figures than the two-dimensional configuration. Geometry parametric studies were also conducted, showing that an increase in the number of ramps benefited engine performance, whereas an increase in compression ratio worsened it. Shorter isolator lengths were also found to improve performance, but at the cost of flow uniformity at the combustor entrance. A higher contraction ratio led to inlet unstart for the two-dimensional configuration but seemed to improve performance for the axisymmetric one. A rounded expansion corner was also found to reduce performance. Lastly, both configurations were found to be able to operate at Mach 7, at the cost of lower engine performance.

References

[1] J. D. Anderson, *Hypersonic and High-Temperature Gas Dynamics*. AIAA Education Series, 2006. ISBN:978-1563477805.

[2] W. H. Heiser and D. T. Pratt, *Hypersonic Airbreathing Propulsion*. AIAA Education Series, 1994. ISBN:978-1563470356.

[3] L. H. Quan, N. P. Hung, L. D. Quang, and V. N. Long, "Analysis and design of a scramjet engine inlet operating from Mach 5 to Mach 10," *International Journal of Mechanical Engineering and Applications*, vol. 4, pp. 11–23, Feb. 2016.

[4] S. kyun Im and H. Do, "Unstart phenomena induced by flow choking in scramjet inlet-isolators," *Progress in Aerospace Sciences*, vol. 97, pp. 1–21, 2018.

[5] R. S. Fry, "A century of ramjet propulsion technology evolution," *Journal of Propulsion and Power*, vol. 20, pp. 27–58, Jan-Feb 2004. doi:10.2514/1.9178.

[6] J. Urzay, "Supersonic Combustion in Air-Breathing Propulsion Systems for Hypersonic Flight," *Annual Review of Fluid Mechanics*, vol. 50, pp. 593–627, Jan. 2018.

[7] D. Andreadis, "Scramjet engines enabling the seamless integration of air and space operations." Pratt and Whitney.

[8] M. K. Smart, "Scramjet inlets." Centre for Hypersonics, The University of Queensland.

[9] A. Tahsini, "Combustion efficiency and pressure loss balance for the supersonic combustor," *Proceedings of the Institution of Mechanical Engineers, Part G: Journal of Aerospace Engineering*, vol. 234, no. 6, pp. 1149–1156, 2019.

[10] G. E. Palmer and M. J. Wright, "Comparison of methods to compute high-temperature gas viscosity," *Journal of Thermophysics and Heat Transfer*, vol. 17, Apr-Jun 2003.

[11] F. G. Blottner, M. Johnson, and M. Ellis, "Chemically reacting viscous flow program for multicomponent gas mixtures," Jan. 1971.

[12] G. Palmer and M. Wright, "A comparison of methods to compute high-temperature gas thermal conductivity," in *36th AIAA Thermophysics Conference*.

[13] C. Park, "Review of chemical-kinetic problems of future NASA missions. I - Earth entries," *Journal of Thermophysics and Heat Transfer*, vol. 7, no. 3, pp. 385–398, 1993.

[14] C. Park, "Two-temperature interpretation of dissociation rate data for N_2 and O_2," *26th Aerospace Sciences Meeting*, Jan. 1988.

[15] E. Curran and S. Murthy, *Scramjet Propulsion*. Progress in Astronautics and Aeronautics, American Institute of Aeronautics and Astronautics, 2000.

[16] D. Herrmann, F. Siebe, and A. Gülhan, "Pressure fluctuations (buzzing) and inlet performance of an airbreathing missile," *Journal of Propulsion and Power*, vol. 29, no. 4, pp. 839–848, 2013.

[17] K. R. Sekar, S. K. Karthick, S. Jegadheeswaran, and R. Kannan, "On the unsteady throttling dynamics and scaling analysis in a typical hypersonic inlet–isolator flow," *Physics of Fluids*, vol. 32, no. 12, p. 126104, 2020.